Quantifying protocol efficiency: A thermodynamic figure of merit for classical and quantum state-transfer protocols

Qiongyuan Wu,[1] Mario A. Ciampini,[2] Mauro Paternostro,[1] and Matteo Carlesso[1,*]

[1]*Centre for Quantum Materials and Technologies, School of Mathematics and Physics, Queen's University Belfast, Belfast BT7 1NN, United Kingdom*

[2]*University of Vienna, Faculty of Physics, Vienna Center for Quantum Science and Technology (VCQ), A-1090 Vienna, Austria*

(Received 23 December 2022; accepted 28 March 2023; published 24 May 2023)

Manipulating quantum systems undergoing non-Gaussian dynamics in a fast and accurate manner is becoming fundamental to many quantum applications. Here, we focus on classical and quantum protocols transferring a state across a double-well potential. The classical protocols are achieved by deforming the potential, while the quantum ones are assisted by a counterdiabatic driving. We show that quantum protocols perform more quickly and accurately. Finally, we design a figure of merit for the performance of the transfer protocols—namely, the *protocol grading*—that depends only on fundamental physical quantities, and which accounts for the quantum speed limit, the fidelity, and the thermodynamics of the process. We test the protocol grading with classical and quantum protocols, and show that quantum protocols have higher protocol grading than the classical ones.

DOI: 10.1103/PhysRevResearch.5.023117

I. INTRODUCTION

Advances in the manipulation of Gaussian states and dynamics [1–5] have enabled experimental achievement in quantum sensing [6,7], communication, and computation [8–10]. However, a framework based only on Gaussian states is inadequate for universal quantum computation [11,12], for instance, with the availability of suitable non-Gaussian resources being a necessary ingredient to unlock the potential of continuous-variable quantum information processing [13–17]. Recent improvements have demonstrated the viability of generation and manipulation of non-Gaussian systems in platforms such as nonlinear optics, ultracold atoms [18], (opto- and electro)mechanical systems [19,20], and superconducting systems [21]. A simple, nearly platform-agnostic paradigm for the engineering of non-Gaussian states is embodied by the *double-well potential* [22,23], whose richness and effectiveness have been proven key in applications of quantum information processing and quantum thermodynamics [24,25].

Quantum control can be successfully deployed in the quest for the generation [26–28] and manipulation [29,30] of non-Gaussian systems. Well-known techniques, from feedback control [31–33] to optimal control [34] and shortcut-to-adiabaticity (STA) [35,36] are generally designed to optimize different aspects of a quantum process, while the possibility to achieve enhanced performances—above and beyond those characterizing their classical counterparts [9,37–39]—through the combination of multiple techniques has been investigated [40–42]. Among them, STA protocols aim at minimizing the leakage into high-excitation subspaces that would be inevitably entailed by the fast dynamics of a quantum system, thus mimicking an *adiabatic* process that would otherwise be unachievable. A relevant form of STA protocols is counterdiabatic driving (CD) [43,44], which has acquired popularity owing to its simple structure that makes it readily implementable in problems of system translation [45,46], state engineering [47,48], and open systems dynamics [49,50].

The development of effective control techniques has not been accompanied by a concomitant effort aimed at the identification of comprehensive quantifiers to measure the advantages and costs of implementing quantum control. Yet, the availability of such a figure of merit—which should allow the characterization of the quality of a protocol—would allow the comparison of performances of different processes implemented with different approaches.

Motivated by the need to provide a physically motivated figure of merit that is able to capture the facets of a quantum control protocol and inform against relevant performance indicators, here we put forward a quantifier, which we dub the *protocol grading parameter*, built around fundamental quantities such as speed of performance of a protocol, fidelity of implementation, and entropic cost. Our proposed tool is able to holistically assess the implications of embedding quantum control approaches into a given dynamical process, thus informing the selection of the best protocol to apply to a given problem among different ones that might be available. We benchmark our proposal by applying a CD scheme to a quantum system trapped in a double-well potential and addressing the performance of (accelerated) quantum-control-enhanced state transfer. The choice of our paradigm problem is relevant from a number of viewpoints. First, by reinterpreting

*m.carlesso@qub.ac.uk

TABLE I. Definitions of the terms entering the protocol grading $\mathcal{G}$ that is defined in Eq. (1): g_S describes the energetic cost, g_Q expresses the experimental quality, while g_T accounts for the thermodynamical cost. Details on their construction are reported in Secs. II A, II B, and II C, respectively.

Quantity	Definition
g_S	$\max\left\{0,\ 1-0.1\times\log_{10}\left(\frac{\tau}{\tau_{QSL}}\right)\right\}$
g_Q	$F_{expt}(\rho_f,\rho_{TG})$
g_T	$\exp\left(-\Sigma_{ir}\right)$

the process of transferring a quantum mechanical system across a double well as the backbone of a *logical resetting* mechanism, our analysis can provide a characterization of any logical operation that does not rely explicitly on Landauer-like arguments but focuses on an inherently dynamical approach. Second, by assessing speed, reliability, and energetic cost of dynamical switching, our figure of merit and study will be instrumental to the furthering of the current effort dedicated to the characterization of quantum memories [51–53], providing key information for their experimental implementation.

The remainder of this paper is structured as follows. In Sec. II, we design the protocol grading to quantify the performances of such protocols, and discuss the fundamental quantities used as its building blocks. In Sec. III, we define the task of transferring the state of a quantum system across a double-well potential, and introduce four protocols for its implementation. In Sec. IV, we simulate the protocols using methods developed in Ref. [54], while we discuss their performance in Sec. V. Finally, in Sec. VI we draw our conclusions.

II. PROTOCOL GRADING

The main aim of this work is to grade the protocols through the newly introduced *protocol grading parameter*, which we will indicate with $\mathcal{G}$, based on the following idea. If the state transfer protocol (1) performs quickly, (2) consumes a small amount of energy, (3) produces faithful results, and (4) has a low degree of irreversibility, it would be considered successful. Correspondingly, $\mathcal{G}$ would achieve its largest possible value (in the following, we will normalize our figure of merit so that $\mathcal{G}\in[0,1]$). Conversely, if the above performance indicators are not met, the protocol will be considered to perform poorly, and we associate it to a low value of $\mathcal{G}$ (close to zero). Our analysis thus explicitly takes into consideration the quantum speed limit g_S, experimental quality g_Q, and thermodynamic cost g_T of the protocol. It is thus natural to construct the quantity

$$\mathcal{G}=g_S g_Q g_T. \tag{1}$$

The form of g_S, g_Q, and g_T are summarized in Table I, and they are explicitly discussed below. We can anticipate that they depend only on universal fundamental quantities, and thus $\mathcal{G}$ can be employed to quantify the quality of the transfer protocol independently from the scheme and the platform where it is performed.

A. Quantum speed limit g_S

We consider as the first quality the protocol time. Here, inspired from information processing, the shorter the better. Shorter timescales are also beneficial for having reduced interaction with the environment, and thus lower decoherence [55,56]. The time to implement the protocol has a fundamental lower bound determined by the quantum speed limit (QSL) [57], which imposes a minimum time τ_{QSL} to be able to distinguish two states during an evolution. For a closed dynamics with time-independent Hamiltonian, the QSL imposes the following bound on a quantum evolution [57]:

$$\tau\geqslant\max\left\{\frac{\hbar}{\Delta E_\tau}\mathcal{L}(\rho_i,\rho_f),\frac{2\hbar}{\pi\langle E\rangle_\tau}\mathcal{L}(\rho_i,\rho_f)^2\right\}, \tag{2}$$

where $\langle E\rangle_\tau$ is the time-averaged mean energy, and ΔE_τ is the time-averaged energy variance. $\mathcal{L}(\rho_i,\rho_f)$ is the Bures angle between the initial state ρ_i and the final state ρ_f, and it is defined as

$$\mathcal{L}(\rho_i,\rho_f)=\arccos\left(\sqrt{F(\rho_i,\rho_f)}\right), \tag{3}$$

where $F(\rho_i,\rho_f)$ is the quantum fidelity, which reads

$$F(\rho_i,\rho_f)=\mathrm{Tr}\left\{\sqrt{\sqrt{\rho_i}\rho_f\sqrt{\rho_i}}\right\}^2. \tag{4}$$

The Bures angle serves to quantify the distance between two states. The two expressions compared in Eq. (2) are respectively the Mandelstam-Tamm limit [58] and the Margolus-Levitin limit [59]. It can be shown that the maximum between these limits provides the proper upper bound to the QSL [60]. A generalization of the QSL in Eq. (2) has been introduced to generic open positive dynamics with time-dependent Hamiltonian [61], such that

$$\tau\geqslant\max\left\{\frac{1}{\Lambda_\tau^{op}},\frac{1}{\Lambda_\tau^{hs}},\frac{1}{\Lambda_\tau^{tr}}\right\}\hbar\sin^2[\mathcal{L}(\rho_i,\rho_f)], \tag{5}$$

where $\{\Lambda_\tau^{op},\Lambda_\tau^{hs},\Lambda_\tau^{tr}\}$ are the time-averaged operator, and Hilbert-Schmidt and trace norms, respectively. Here, we decide to use the bound tightened by the Hilbert-Schmidt norm $\|A\|_{hs}=\sqrt{\mathrm{Tr}\{A^\dagger A\}}$, which is linked to the Mandelstam-Tamm limit in closed dynamics, due to its connection to the energetic cost associated with implementing the shortcut in Hamiltonian $H_1(t)$ [62,63]; namely, we take

$$\tau_{QSL}=\frac{\hbar}{\Lambda_\tau^{hs}}\sin^2[\mathcal{L}(\rho_i,\rho_f)], \tag{6}$$

where $\Lambda_\tau^{hs}=\frac{1}{\tau}\int_0^\tau dt\|L[\rho_t]\|_{hs}$ and $L[\rho_t]$ is the generator of the dynamics [this will be eventually the right-hand side of Eq. (12)].

Given that $\tau\geqslant\tau_{QSL}$, we quantify the speed g_S with the following coarse-grained function,

$$g_S=\max\left\{0,\left(1-0.1\times\log_{10}\frac{\tau}{\tau_{QSL}}\right)\right\}, \tag{7}$$

which measures the magnitude of the ratio between τ and τ_{QSL}. In particular, we make the speed quality decrease by 0.1 when the ratio increases one order of magnitude. To make an explicit example, if $\tau/\tau_{QSL}\sim1$ then $g_S\approx1$; if $\tau/\tau_{QSL}\sim10$ then $g_S\approx0.9$, etc. The definition of g_S we consider automatically sets g_S to zero for any protocol requiring a time τ being

equal to or larger than $10^{10}\tau_{\rm QSL}$. This can be considered a flaw of the definition. However, alternative definitions of $g_{\rm S}$, such as $\tau_{\rm QSL}/\tau$, would not give proper weight to really good protocols (e.g., $\tau = 10^2\tau_{\rm QSL}$). Notice that $\tau_{\rm QSL}$ is determined by the generalized time-averaged energy variance (i.e., $\Lambda^{\rm hs}_\tau$) and the distance between the initial and final states (i.e., $\sin^2[\mathcal{L}(\rho_i, \rho_f)]$). This means that for an efficient protocol, one needs to have a small value of $\Lambda^{\rm hs}_\tau\tau/\sin^2[\mathcal{L}(\rho_i, \rho_f)]$.

B. Experimental quality $g_{\rm Q}$

The goal of the protocol is to transfer a state from one to the other well of a double-well potential. The quality of the protocol is reflected by how much the final state ρ_f after having run the protocol is near the target state $\rho_{\rm TG}$ of the protocol task. Thus, we choose to quantify the experimental quality $g_{\rm Q}$ with the fidelity F between these two states:

$$g_{\rm Q} = F_{\rm expt}(\rho_f, \rho_{\rm TG}). \tag{8}$$

We add the subscript expt to stress that such a fidelity is also subject to experimental imperfections (such as those imposed by the statistical and systematic errors), and performing these protocols in real experiments would usually result in states with lower fidelity compared to the theoretical one. Here, we focus only on the later fidelity, which is given by the action of the protocol.

The protocol task and its target state $\rho_{\rm TG}$ are defined as follows. We consider the double-well potential as divided into two local potentials, and we denote respectively with $\{|j(t)\rangle_{\rm L}\}$ and $\{|j(t)\rangle_{\rm R}\}$ the corresponding instantaneous eigenstates at time t localized in the left and right wells. We assume that the initial state of the problem is localized in the right well, and thus can be described as a linear superposition of the right instantaneous eigenstates, i.e.,

$$|\psi(0)\rangle = \sum_j \alpha_j\,|j(0)\rangle_{\rm R}\,. \tag{9}$$

In the case where one does not apply the transfer protocol, such a state evolves as

$$|\psi(t)\rangle = \sum_j \alpha_j e^{-iE^{\rm R}_j t/\hbar}\,|j(0)\rangle_{\rm R}\,, \tag{10}$$

where $E^{\rm R}_j$ are the eigenvalues of $H_0(0)$ corresponding to the eigenstate $|j(0)\rangle_{\rm R}$ in the right well. Now, this is the state one would like to have but transferred in the left well. Then, the target state is given by

$$\rho_{\rm TG} = |\phi(\tau)\rangle\,\langle\phi(\tau)|\,,$$

where

$$|\phi(\tau)\rangle = \sum_j \alpha_j e^{-iE^{\rm R}_j \tau/\hbar}\,|j(0)\rangle_{\rm L}\,, \tag{11}$$

where the relative weights α_j and the energies $E^{\rm R}_j$ are the same as in Eq. (10), but its decomposition is done on the left instantaneous eigenstates $|j(0)\rangle_{\rm L}$. In such a way, the state $|\phi(\tau)\rangle$ in Eq. (11) has the same information content of the state $|\psi(t=\tau)\rangle$ in Eq. (10), and one can say that the state has been perfectly transferred.

C. Thermodynamic cost $g_{\rm T}$

In experiments, the system is always under the influence of environment, and unavoidably undergoes nonequilibrium processes if the protocol is performed in a finite time. To account for such effects, we consider the following master equation:

$$\dot\rho = -\frac{i}{\hbar}[H_{\rm sys}, \rho] + D_{\rm lc}[\rho] + D_{\rm th}[\rho], \tag{12}$$

where $D_{\rm lc}[\rho]$ and $D_{\rm th}[\rho]$ are respectively the localization and thermal dissipators. The first one describes the decoherence due to photon recoil [64], which has the form [65]

$$D_{\rm lc}[\rho] = -\Lambda[x, [x, \rho]], \tag{13}$$

where Λ is the corresponding diffusion constant. The thermal effects of the interactions with an environment with a temperature T are instead accounted by $D_{\rm th}[\rho]$, which is a complete positive version of the Caldeira-Leggett dissipator reading [66–69]

$$D_{\rm th}[\rho] = -\frac{i\gamma}{2\hbar}[x, \{p, \rho\}] - \sum_{q=x,p}\gamma_q[q, [q, \rho]] \tag{14}$$

with $\gamma_x = \gamma m k_{\rm B}T/\hbar^2$ and $\gamma_p = \gamma/(16 m k_{\rm B}T)$. Here γ is the coupling strength with the environment, m is the mass of the particle, and $k_{\rm B}$ is the Boltzmann constant.

The interaction with the environment results in an irreversible entropy production $\Sigma_{\rm ir} \geqslant 0$ [70], which would be redeemed with exchanging heat between the system and the environment during the thermalization. Usually this indicates that the process is no longer time reversible and that the system information is lost. To quantify such a thermodynamic cost, we use

$$g_{\rm T} = e^{-\Sigma_{\rm ir}}, \tag{15}$$

which resembles the expression from fluctuation theorems [71–74], and it favors the process with small irreversible entropy production.

By building on the results of our previous work [54], we use the Wehrl entropy to measure the above quantity, which reads [75]

$$S_{\mathcal{Q}} = -\int d\alpha \int d\alpha^*\,\mathcal{Q}_\rho(\alpha, \alpha^*)\ln\mathcal{Q}_\rho(\alpha, \alpha^*), \tag{16}$$

where $\mathcal{Q}_\rho(\alpha, \alpha^*)$ is the Husimi Q function being defined in terms of the coherent state $|\alpha\rangle$:

$$\mathcal{Q}_\rho(\alpha, \alpha^*) = \frac{1}{\pi}\,\langle\alpha|\,\rho\,|\alpha\rangle\,. \tag{17}$$

In the case under study, one does not have a harmonic potential and thus the coherent states $|\alpha\rangle$ are more difficult to define. Nevertheless, for low energies, one can approximate the single well as a harmonic oscillator with frequency $\omega = (E_1 - E_0)/\hbar$, where E_0 and E_1 are respectively the ground and first-excited-state energies of one of the two wells. In such a way, one can define the creation and annihilation operators $a^\dagger$ and a through $x = \sqrt{\frac{\hbar}{2m\omega}}(a + a^\dagger)$, $p = -i\sqrt{\frac{\hbar m\omega}{2}}(a - a^\dagger)$; the corresponding coherent states $|\alpha\rangle$ follow straightforwardly.

We note that the final result for the irreversible entropy production does not depend on the choice of ω, underlying the strength of this reasoning.

Conversely to the von Neumann entropy, the Wehrl entropy has well-defined decomposed rates at the zero-temperature limit, and is the upper bound to the von Neumann entropy [75–78]. To compute the irreversible entropy production $\Sigma_{\rm ir}$, we first take the time derivative of the Wehrl entropy. Given the master equation in Eq. (12), we can decompose the latter as

$$\frac{dS_{\mathcal{Q}}}{dt} = \frac{dS_{\mathcal{U}}}{dt} + \frac{dS_{\mathcal{D}_{\rm lc}}}{dt} + \frac{dS_{\mathcal{D}_{\rm th}}}{dt}, \tag{18}$$

where the first term is the Wehrl entropy rate for the unitary process, and the two other terms are the rates for the dissipative processes. In general, one can decompose the rate of a dissipative process as

$$\frac{dS_{\mathcal{D}}}{dt} = \Pi - \Phi, \tag{19}$$

where the first term Π is the irreversible entropy production rate, and the second term Φ is the entropy flux rate. It follows that the total irreversible entropy production during the process is

$$\Sigma_{\rm ir} = \int_0^\tau dt\, \Pi(t). \tag{20}$$

Here, the irreversible entropy production rate Π comes from the component that is even to the time reversal of the entropy rate, and the entropy flux rate Φ comes from the component that is odd [79]. It has been shown [78] that for a dissipator of the form

$$D[\rho] = -[O,[O,\rho]], \tag{21}$$

with $O = x$ or p, one has solely the irreversible entropy production rate, which is given by

$$\Pi = \int d\alpha \int d\alpha^* \frac{|\mathcal{C}_O(\mathcal{Q})|^2}{\mathcal{Q}}, \tag{22}$$

and depends on the even power of the current $\mathcal{C}_O(\mathcal{Q}) = \langle\alpha|[O,\rho]|\alpha\rangle$. In this way, one can account for the dissipator $D_{\rm lc}[\rho]$ and the last two terms of $D_{\rm th}[\rho]$ as defined in Eq. (14). On the other hand, the first term of $D_{\rm th}[\rho]$ needs to be tackled in a different way. We show in Appendix B that it can be decomposed in two parts as

$$-\frac{i\gamma}{2\hbar}[x,\{p,\rho\}] = -\frac{\gamma}{2\hbar}[x,[x,\rho]] - \frac{\gamma}{\sqrt{2}\hbar}[x,\rho a - a^\dagger \rho]. \tag{23}$$

In particular, the first part has the form appearing in Eq. (21) and thus it contributes to the irreversible entropy production rate Π only. The second part contributes instead to the entropy flux rate, since it corresponds a contribution to the entropy rate Φ that is odd in the current (cf. Appendix B). Therefore, the explicit expressions of the total irreversible entropy production and the flux rates of the model in Eq. (12) are

$$\begin{aligned}\Pi &= \left(\frac{\gamma}{2\hbar} + \gamma_x + \Lambda\right)\int d\alpha \int d\alpha^* \frac{|\mathcal{C}_x(\mathcal{Q})|^2}{\mathcal{Q}} \\ &\quad + \gamma_p \int d\alpha \int d\alpha^* \frac{|\mathcal{C}_p(\mathcal{Q})|^2}{\mathcal{Q}}, \\ \Phi &= \frac{\gamma}{\sqrt{2}\hbar}\int d\alpha \int d\alpha^* \,|\alpha|^2\, \mathcal{C}_x(\mathcal{Q}),\end{aligned} \tag{24}$$

from which one can calculate the irreversible entropy production through Eq. (20).

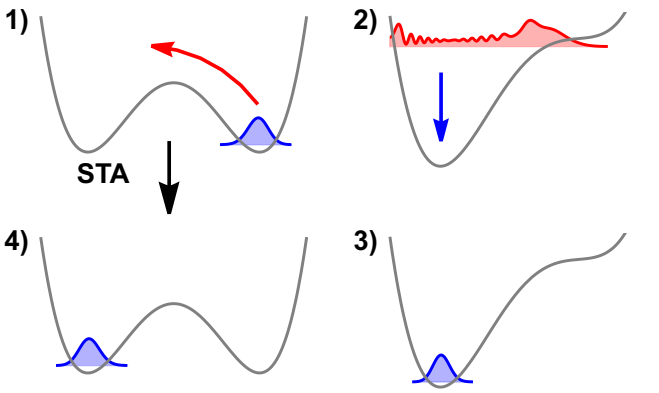

FIG. 1. Schematic illustration of the classical and the quantum state-transfer protocols. The classical protocol follows the frame sequence $1 \to 2 \to 3 \to 4$, while the quantum protocol goes directly from $1 \to 4$ with the help of STA.

III. PROTOCOLS FOR THE STATE TRANSFER

In order to showcase the use of the protocol grading that we defined in Sec. II, here we consider the specific problem of transferring a state from one side to the other of a double-well potential. We consider a one-dimensional system in a double-well potential, whose corresponding Hamiltonian reads

$$H_{\rm free} = \frac{p^2}{2m} + c_1 x^2 + c_2 x^4, \tag{25}$$

where the coefficients $c_1 < 0$ and $c_2 > 0$ determine the shape of the double-well potential. Next, we will introduce two particular classical protocols and two quantum ones for the state transfer. The classical protocols only deform the potential, and the state must go over the barrier to reach the other side. Conversely, the quantum protocols harness genuine quantum effects, namely, the quantum tunneling, such that the state transfers through the barrier between the two wells with the help of the counterdiabatic term. A schematic illustration of the protocols is shown in Fig. 1.

A. Classical state transfer

In order to switch the state of a trapped particle from the left to the right well, we allow an external agent to modify the potential through an external control term that is added up to $H_{\rm free}$ as

$$H_0(t) = H_{\rm free} + f(x,t). \tag{26}$$

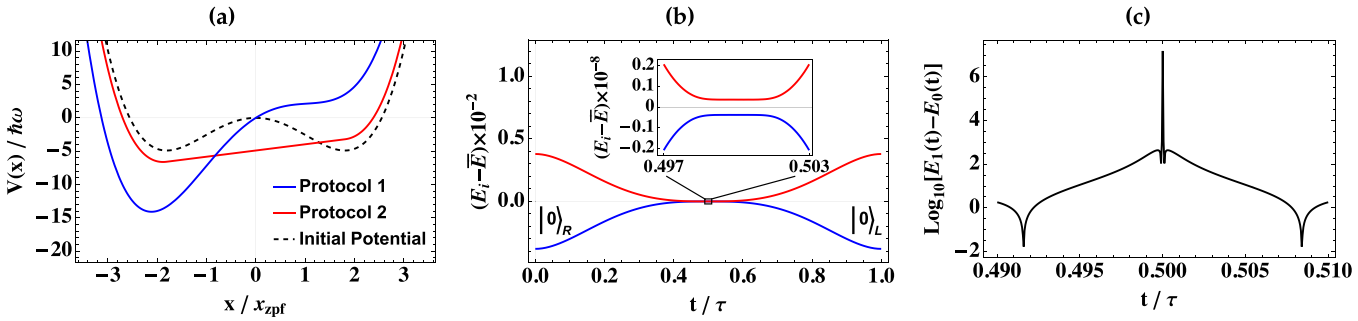

FIG. 2. (a) The shapes of the trapping potentials for the two classical protocols implemented with $f_1^{\mathrm{C}}(x,t)$ and $f_2^{\mathrm{C}}(x,t)$, respectively shown as blue and red lines, compared to the initial potential at $t=0$ represented with a black dashed line. Here, we set $x_{\mathrm{zpf}}=\sqrt{\hbar/2m\omega}$, with $\omega\approx 2.3$, $c_1=-1.5$, $c_2=0.05$, $\delta=0.001$, and $a_1^{\mathrm{C}}=5$, $a_2^{\mathrm{C}}=b_2^{\mathrm{C}}=1$; the time t is set to that maximizing the change in the potential. (b) The dynamics of the ground (blue line) and first-excited (red line) energies of $H_0(t)$ with the control parameter $f_2^{\mathrm{Q}}(x,t)$, whose value changes from $-\delta x$ to δx over a time window $t\in[0,\tau]$. As one can see, their distance is of the order of 10^{-9} in the central part of the protocol (see inset). (c) The difference between the first-excited and ground state when applying the STA protocol [in particular that with the control parameter described in Eq. (32) below]. The energy difference in the center of the protocol ($t=\tau/2$) is now big, $\sim 10^7$. Two minima of such a difference appear on the sides of the center with a value of the order of 10^{-2}, which is still seven orders of magnitude larger than the absolute minimum of the energy difference in the classical protocol.

The role of $f(x,t)$ is to deform the potential. We consider two classical transfer protocols, which correspond to the following control functions:

$$f_1^{\mathrm{C}}(x,t)=\alpha_1^{\mathrm{C}}(t)x, \tag{27}$$

$$f_2^{\mathrm{C}}(x,t)=\alpha_2^{\mathrm{C}}(t)x-\beta_2^{\mathrm{C}}(t)\left(\frac{c_1^2}{4c_2}+c_1x^2+c_2x^4\right)\times\theta\left(-\frac{c_1}{2c_2}-x^2\right). \tag{28}$$

The first control function simply tilts the potential by adding a linear term $\alpha_1^{\mathrm{C}}(t)x$ to the potential. We choose the parameter $\alpha_1^{\mathrm{C}}(t)$ to change linearly in time from $-\delta<0$ to $A_1>0$. Here, the positive value of δ is small but nonzero which is needed to make the initial potential asymmetric (slightly tilted towards the right side), so that the ground state of the system is initially localized in the right well. The value of A_1 determines the degree of the maximal tilting. The second considered control function, in addition to the linear tilting process controlled by $\alpha_2^{\mathrm{C}}(t)\in[-\delta,A_2]$, adds another term that linearly flattens the central part of the double-well potential (namely, the wall between the two wells), and it is controlled by $\beta_2^{\mathrm{C}}(t)\in[0,1]$. Such a choice has already been experimentally realized with trapped underdamped nano- and microparticles in the classical, stochastic regime [80–82]. These two protocols implement the transfer in two structurally different ways. In short, the first classical protocol just tilts the potential, while the second one tilts it and flattens its central part. In Fig. 2(a), we compare the two potentials at the time of the corresponding strongest imposed tilting.

The first classical protocol (dubbed classical protocol 1) is illustrated in Fig. 1 with the frame sequence $1\to2\to3\to4$ and it is implemented as follows. We assume that the system is initially localized in the ground state in the right well (cf. frame 1) and we want to transfer it to the ground state of the left well (cf. frame 4). When acting on the system with the control function $f_1(x,t)$, the energy of the system unavoidably grows due to the nonadiabatic deformation of the potential, and thus high-energy states of system get populated (cf. frame 2). Since the high-energy wavefunctions extend over the entire potential, the position of the system is no longer localized, as shown by the red wave packet in frame 2. To drive the system back to the ground state (which is now in the left well) (cf. frame 3), we need to cool down the system. This can be done by attaching it to an environment at low temperatures, so that after some time the system will dissipate heat to the environment. In particular, we attach the latter to the system already at the beginning of the protocol at time $t=0$. In general, the energy increase is large when a fast tilting is performed, while in an adiabatic (infinite time) process it is smaller although lower bounded by a generalized Landauer principle [80,83,84]. A fast tilting process is usually not desired due to the large energy increase and the consequent long-time cooling needed. Finally, one can reverse the protocol, namely, run the control functions backwards, and restore the initial potential (cf. frame 4), which completes the classical transfer protocol.

The second classical protocol (which we refer to as classical protocol 2) works in a similar manner as the first one. Again, the frame sequence the system will follow is given by $1\to2\to3\to4$, with the only difference being that the potential is not only tilted but also flattened in its central part [see, for instance, the red line in Fig. 2(a)]. Again, there will be a heating of the system due to the tilting and flattening, which will lead to a spread of the wave packet and it will require a cooling process.

B. Quantum state transfer

To construct the quantum state transfer protocol, we start from the Hamiltonian $H_0(t)$ considered for the classical protocol in Eq. (26). For the sake of simplicity, here we consider the application of STA only to the first classical protocol. Indeed, STA does not apply well to the second protocol due to the degeneracy between the energies of the left and right wells appearing when the potential is flattened [36,85].

The quantum part of classical protocol 1 is implemented through the assistance of STA. In particular, a CD driving such as the one defined in Refs. [36,43] is introduced through the following:

$$H_1(t) = H_0(t) + H_{\rm STA}(t), \tag{29}$$

where we included the counterdiabatic term, which reads $H_{\rm STA}(t) = i\hbar \sum_i [|\partial_t i\rangle \langle i| , |i\rangle \langle i|]$, where $|i\rangle = |i(t)\rangle$ are the instantaneous eigenstates of the Hamiltonian H_0 with corresponding energies $E_i = E_i(t)$, such that $H_0(t)|i(t)\rangle = E_i(t)|i(t)\rangle$. The explicit form of $|\partial_t i\rangle$ can be computed with the Schrödinger equation [43] and thus $H_{\rm STA}$ can be recast as

$$H_{\rm STA}(t) = i\hbar \sum_{i\neq j} \frac{\langle i|\dot{H}_0|j\rangle}{E_j - E_i} |i\rangle\langle j| . \tag{30}$$

In order to ensure that the initial and final potentials are those of the original Hamiltonian H_0, we impose the STA conditions $H_{\rm STA}(0) = H_{\rm STA}(\tau) = 0$ on the CD term.

The quantum protocol we consider here is similar to that in Ref. [86], where the protocol exploits the tunneling effect in a double-well potential. Here, we adopt the STA to achieve and accelerate the state transfer. In particular, the protocol works due to the following reasons: (i) the sign change of the control parameter $f(x,t) \in [-\delta x, \delta x]$ flips the asymmetry of the potential in Eq. (26), switching the ground state from being in right well to the left well (see a simple application to the Landau-Zener model in Appendix A), and (ii) the solutions of the new Hamiltonian $H_1(t)$ follow, in finite time τ, the adiabatic trajectory of the original Hamiltonian H_0. In Fig. 2(b), we plot the dynamics of the eigenvalues for the ground state (in blue) and first-excited state (in red) of H_0. In the classical protocol, when starting from the ground state in the right well $|0\rangle_{\rm R}$ and moving towards that in the left $|0\rangle_{\rm L}$, due to the energy increase, the system will jump from the ground state to the first-excited one (i.e., from the blue to the red line) when the energy gap is small enough (this happens at $t/\tau = 0.5$). To prevent this, the quantum protocol increases the energy gap between the ground and the first-excited state, as depicted in Fig. 2(c). In such a way, it is more difficult to excite the system [62], at the cost of extra energy input given by the CD term. Therefore, the quantum protocol works as follows: we prepare the system in the ground state in the right well $|0\rangle_{\rm R}$, then the system evolves with the new Hamiltonian $H_1(t)$ and will follow the blue line, resulting in the ground state in the left well $|0\rangle_{\rm L}$ (as depicted by the frame sequence $1 \to 4$ in Fig. 1).

We start with the system prepared in the ground state in the right well with the control parameter set to $f_i^{\rm Q}(x,0) = -\delta x$. The state transfer is performed with the new Hamiltonian $H_1(t)$ and modifying the control parameter to a positive value $f_i^{\rm Q}(x,\tau) = \delta x$. The way that $f_i^{\rm Q}(x,t)$ is changed is determined by the STA conditions. Here we consider the control parameter to be proportional to the position operator as in Eq. (27):

$$f_i^{\rm Q}(x,t) = \alpha_i^{\rm Q}(t)x. \tag{31}$$

The substitution of the latter expression in Eq. (26) gives $\dot{H}_0 = \dot{\alpha}_i(t)x$ which is then merged with Eq. (30). Eventually, $H_{\rm STA}(t)$ will be computed numerically (cf. Sec. IV). To the best of our knowledge, an analytical expression of such a counterdiabatic term in a tilting double-well potential is still unknown, while preliminary studies to attain its analytical expression in a similar double-well potential can be found in Refs. [87,88]. The STA conditions impose $\dot{\alpha}_i(0) = \dot{\alpha}_i(\tau) = 0$. This considered, one can construct different interpolation of the control parameter connecting $\alpha_i^{\rm Q}(0) = -\delta$ to $\alpha_i^{\rm Q}(\tau) = \delta$. Indeed, it has been shown that the energy cost of the counterdiabatic term $H_{\rm STA}$ can be reduced by optimizing the control parameter [89]. The first option we consider is a control parameter that is cubic in time and it is described by

$$\alpha_1^{\rm Q}(t) = -\delta + \frac{6\delta t^2}{\tau^2} - \frac{4\delta t^3}{\tau^3}. \tag{32}$$

We indicate this control scheme to be linear as it grows linearly at $t = \tau/2$; this is when the energy gaps of $H_0(t)$ are the smallest [e.g., when the potential of H_0 is symmetric, and the denominator in Eq. (30) is smallest, making at that time the contribution of $H_{\rm STA}$ the largest]. In the second quantum protocol, we further require that $\dot{\alpha}_2^{\rm Q}(\tau/2) = 0$. In contrast with the linear interpolation in Eq. (32), this gives the following nonlinear behavior of the control parameter:

$$\alpha_2^{\rm Q}(t) = -\delta + \frac{30\delta t^2}{\tau^2} - \frac{100\delta t^3}{\tau^3} + \frac{120\delta t^4}{\tau^4} - \frac{48\delta t^5}{\tau^5}. \tag{33}$$

In summary, we have introduced two options for classical state transfer, namely, $f_1^{\rm C}(x,t)$ and $f_2^{\rm C}(x,t)$, and two options for quantum state transfer, $f_1^{\rm Q}(x,t)$ and $f_2^{\rm Q}(x,t)$. In particular, $f_1^{\rm C}(x,t)$ and $f_1^{\rm Q}(x,t)$ are the simple linear protocols, while $f_2^{\rm C}(x,t)$ and $f_2^{\rm Q}(x,t)$ are nonlinear protocols. We show a sketch of the changes for all control parameters in Fig. 3.

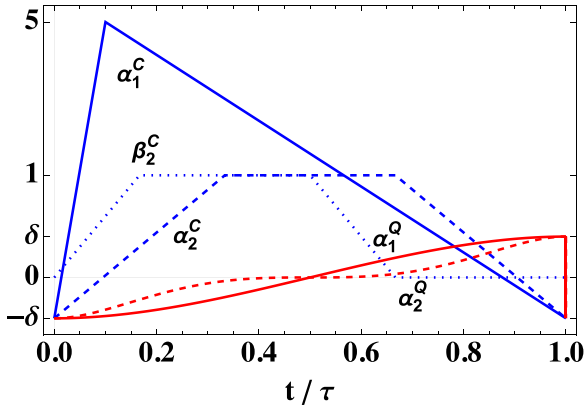

FIG. 3. Schematic illustration of changes of all the functions in the proposed control parameters $f_i^k(x,t)$ with $i = 1, 2$, for the classical $k =$ C and quantum $k =$ Q protocols.

IV. NUMERICAL SIMULATIONS OF TWO PROTOCOLS

In this section, we lay down the basis for corroborating the theoretical framework with numerical simulations, whose basis was described in Ref. [54]. As a case study, we set $c_1 = -1.5$ and $c_2 = 0.05$ [see Fig. 2(a)], where the energy difference between the ground and first-excited states in the right well is $\hbar\omega \approx 2.3$, and let $m = k_{\rm B} = \hbar = 1$. We choose such a potential so that the energetic barrier is high enough to

prepare well-localized states in either of the two wells, while still being low enough to highlight the features of the quantum protocol. Tunable potential landscapes of comparable energy scales have been realized in semiconductor qubits [90], as well as proposed in nanomechanical resonators coupled with quantum dots [91]. Recent experiments with optically levitated nanoparticles provided the necessary toolbox for implementing time-controlled protocols in the quantum regime, as well as quantum-limited position readout and quantum initial state preparation [92,93]. We choose to introduce the following numerical values for the coupling parameters, $\gamma/\omega = 10^{-2}$ and $\Lambda/\omega = 10^{-3}$ from the master equation in Eq. (12), following typical values in such experiments [54]. With this choice of the parameters, the energy at the top of the barrier corresponds to a thermal state with associated temperature $T \approx 12.7$ K. Thus we considered two temperatures, $T = 1$ and 10 K, where the corresponding equilibrium systems have energies below the well potential and are well or loosely localized, respectively. Finally, we consider for all protocols the initial state to be

$$|\psi(0)\rangle = 0.6\,|0\rangle_{\mathrm{R}} + 0.8\,|1\rangle_{\mathrm{R}}\,, \tag{34}$$

and correspondingly the target state at $t = \tau$ given by Eq. (11) reads

$$|\phi(\tau)\rangle = 0.6e^{-iE_0^R\tau/\hbar}\,|0\rangle_{\mathrm{L}} + 0.8e^{-iE_1^R\tau/\hbar}\,|1\rangle_{\mathrm{L}}\,. \tag{35}$$

For the simulations, we use the full toolbox developed in Ref. [54], which is concisely summarized below. The continuous system described by the bosonic field operators $\{a, a^\dagger\}$ can be approximated by a discrete spin-j system with ladder operators $\{J_+, J_-\}$ following the Holstein-Primakoff (HP) transformation, which can be stated as

$$a \approx M_\kappa^{-1} J_+ \quad \text{and} \quad a^\dagger \approx J_- M_\kappa^{-1}, \tag{36}$$

where M_κ is the κth $-$ order Taylor expansion of the nonlinear term in the HP transformation,

$$\hbar\sqrt{2j - a^\dagger a} = M_\kappa + \mathcal{O}((a^\dagger a)^{\kappa+1}). \tag{37}$$

One can define the discretized version of dimensionless quadrature field operators as [2]

$$\begin{aligned} x' &= \frac{1}{\sqrt{2}}\left(J_- M_\kappa^{-1} + M_\kappa^{-1} J_+\right), \\ p' &= \frac{i}{\sqrt{2}}\left(J_- M_\kappa^{-1} - M_\kappa^{-1} J_+\right), \end{aligned} \tag{38}$$

and we have the discretized Hamiltonian,

$$H(t) = \frac{p'^2}{2m} + c_1 x'^2 + c_2 x'^4 + f_{\mathrm{i}}^{\mathrm{k}}(x', t), \tag{39}$$

and the control term can be chosen from $\{f_{\mathrm{i}}^{\mathrm{k}}(x', t)\}_{i=1,2}^{\mathrm{k=C,Q}}$ depending on the specific protocol. Here, the discrete system reflects the low-energy sector of the original continuous system in Eq. (26), which is the sector we focus on. We set the dimension of the system j, as well as the Taylor expansion size κ, to be 60. Namely, we have spin-$\frac{59}{2}$.

On the other hand, the coherent state $|\alpha\rangle$ in a continuous system can be replaced with the spin-coherent state for a discrete system [78],

$$|\Omega\rangle = e^{-i\phi J_z} e^{-i\theta J_y}\,|j, j\rangle\,, \tag{40}$$

where $|j, j\rangle$ is the angular momentum state with largest quantum number of J_z, and $\Omega = \{\theta, \phi\}$ is the set of Euler angles identifying the direction along which the coherent state points. The corresponding Husimi Q function is defined as

$$\mathcal{Q}(\Omega) = \langle\Omega|\,\rho\,|\Omega\rangle\,, \tag{41}$$

the Wehrl entropy for a system with $N = 2j + 1$ degrees of freedom reads

$$S_{\mathcal{Q}} = -\frac{N}{4\pi}\int d\Omega\,\mathcal{Q}(\Omega)\ln\mathcal{Q}(\Omega), \tag{42}$$

and the irreversible entropy production rate in Eq. (24) becomes

$$\begin{aligned} \Pi = &\left(\frac{\gamma}{2\hbar} + \frac{\gamma m k_{\mathrm{B}} T}{\hbar^2} + \Lambda\right)\frac{N}{4\pi}\int d\Omega\,\frac{|J_x(\mathcal{Q})|^2}{\mathcal{Q}} \\ &+ \frac{\gamma}{16 m k_{\mathrm{B}} T}\frac{N}{4\pi}\int d\Omega\,\frac{|J_p(\mathcal{Q})|^2}{\mathcal{Q}}, \end{aligned} \tag{43}$$

where $J_O(\mathcal{Q}) = \langle\Omega|\,[O, \rho]\,|\Omega\rangle$ with $O = x, p$.

A. Classical protocol

The simulations for the classical protocols are performed by employing the Hamiltonian in Eq. (26) with two forms of the control parameter: for protocol 1 we use f_1^{C} defined in Eq. (27), while for protocol 2 we employ f_2^{C} presented in Eq. (28). The control parameters take the values $\delta = 0.001$, $A_1 = 5$, and $A_2 = 1$, and we set $\tau\omega = 300$. As $A_2 < A_1$, protocol 2 tilts the potential less than protocol 1. Indeed, in protocol 2, the central barrier is also lowered; thus the protocol excites less to the system and because of this is the optimized one.

The results of the open dynamics simulations for the two classical protocols are shown in Fig. 4. In Figs. 4(a) and 4(b), we compare the instantaneous numerically solved eigenvalues of $H_0(t)$ defined in Eq. (39) for the continuous (colored lines) and discrete (dashed lines) case for protocol 1 [Fig. 4(a)] and protocol 2 [Fig. 4(b)]. The comparison between the continuous and discrete cases shows that our simulations are accurate in the low-energy sector encompassing the first 15 energy levels. An exception to this is given by the first classical protocol, where the system energy goes slightly beyond this regime [cf. Fig. 4(e)]; then the corresponding results are slightly affected by the approximation. In Figs. 4(c) and 4(d), we show the evolution of the system's position density $|\langle x|\psi(t)\rangle|^2$ along with the time-varying potential undergoing the simple control at 1 K for protocol 1 and protocol 2, respectively. For protocol 1, the deformation of the potential pushes the system to higher energies, which can be seen by the fact that the system is delocalized over the entire potential; i.e., it is not well localized in just one of the two wells. The system is then cooled down during the slow restoration of the potential, due to interaction with the cold environment. In the end, one can see the system is mainly localized in the left well with a distribution close to a Gaussian form, which concludes the state-transfer protocol. For protocol 2 [cf. Fig. 4(d)], the potential is less deformed than that in protocol 1; thus the system gets less excited. Consequently, the final state given by protocol 2 has a higher fidelity to the corresponding thermal state. In the end, one can see the system is mainly localized in the left well and the state transfer is completed.

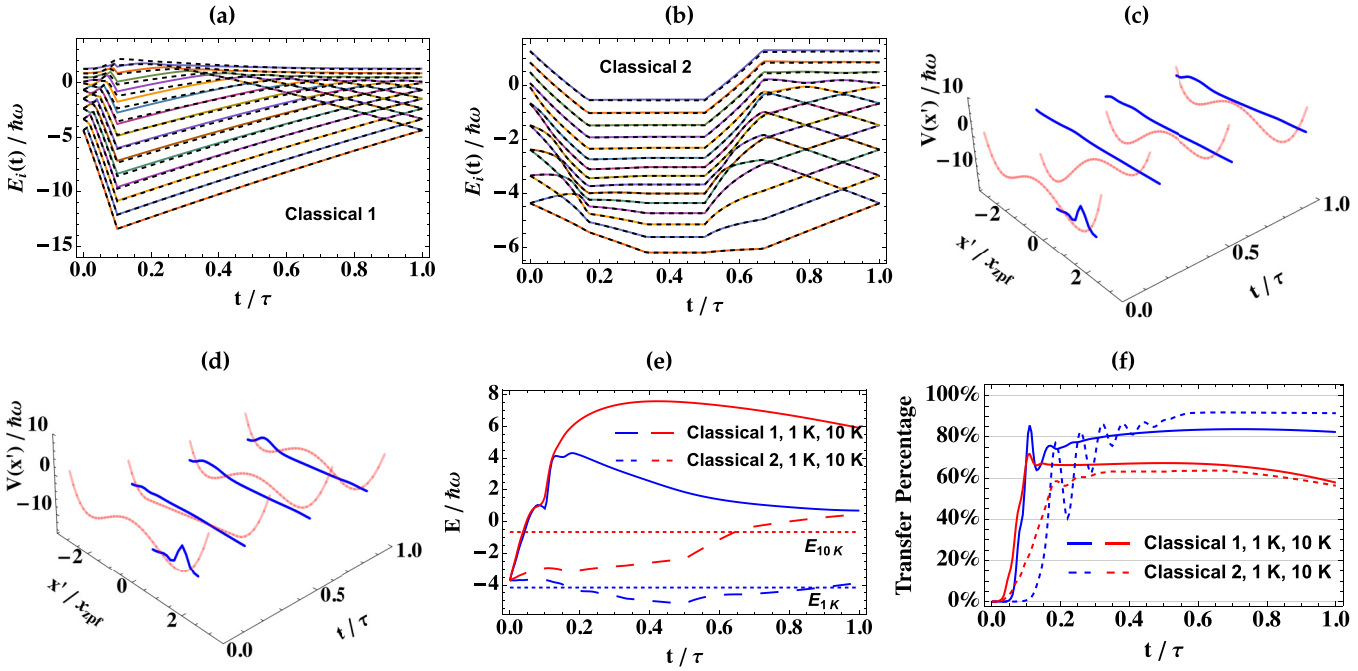

FIG. 4. Classical state-transfer protocols. [(a), (b)] The accuracy of the simulation, by comparing the evolution of the energy levels of the system for the two protocols computed with the continuous (colored lines) and with the discretized (dashed black lines) system. [(c), (d)] The dynamics of the system's density in position (blue line) as the potential (red line) is changed in time at the temperature of 1 K, respectively for classical protocols 1 and 2. The main visible difference between the two panels is in the form of the potential for $t \sim \tau/3$. (e) The system energy $\langle H_0(t)\rangle$ evolution when the system interacts with the environment of different temperatures (1 K in blue and 10 K in red). The continuous and dashed lines correspond to protocol 1 and 2s respectively; the dotted lines correspond to the thermal energies and serve as a reference. (f) The transfer percentage [cf. Eq. (44)] of the system state with respect to the corresponding thermal states. We employed the same color and dashing as in (e).

To quantify the accuracy of the state transfer, we consider the system energy and the transfer percentage. In Fig. 4(e), we show the comparison between the system energies (continuous and dashed lines) and the corresponding thermal energies (dotted lines) serving as references. The lines in blue and red correspond to protocols operating respectively at 1 and 10 K. The continuous lines represent protocol 1, while the dashed ones identify protocol 2. One can see that the final energy is close to the thermal one when protocol 2 is operating at 1 K. This is not the case for protocol 1 when operating at 1 K, neither is it for both protocols at 10 K, at which temperature the thermal state energy is just below the tip of the barrier, and thus the cold bath fails to localize the system in the finite time $\tau\omega = 300$. On the other hand, one can see that protocol 2 operates better than protocol 1 at both temperatures: the system energies grow less and are closer to the corresponding thermal ones. In Fig. 4(f), we report the behavior of the transfer percentage, which is defined as

$$P(x \leqslant 0) = \int_{-\infty}^{0} dx\ \langle x|\rho|x\rangle\,, \tag{44}$$

for protocol 1 and 2 at 1 and 10 K [we use the same color and dashing as in Fig. 4(e)]. At the end of the protocols when the potential is restored to its original shape, the transfer percentage is around 80% for protocol 1 (90% for protocol 2) at 1 K, while it is below 60% for both protocols at 10 K.

B. Quantum protocol

The simulations for the quantum protocols are performed with the CD driving introduced in Eq. (29), where we set $\delta = 0.001$ and $\tau\omega = 10$. We underline the difference of the latter timescale with that considered for the classical protocols in Sec. IV A, which was $\tau\omega = 300$. We consider the environmental action as given by the master equation in Eq. (12) with the values of the parameters being the same as those considered for the classical protocol.

The simulation results are shown in Fig. 5. In Fig. 5(a), we compare the energetic costs of the CD term, which are computed for the quantum protocols [62,63] with

$$\|H_{\rm STA}(t)\| = \sqrt{{\rm Tr}\{H^{\dagger}_{\rm STA}(t)H_{\rm STA}(t)\}}. \tag{45}$$

One can observe that the majority of the cost using $\alpha^{\rm Q}_1(t)$ (blue line) appears around $t = \tau/2$, i.e., when the potential is symmetric. At this time, the CD term enlarges the energy gaps between eigenstates of the system, thus allowing the system to travel along the trajectories with a high speed and without jumping from one trajectory to the other [62]. Conversely, when employing $\alpha^{\rm Q}_2(t)$ (red line), the requirement of $\dot{\alpha}^{\rm Q}_2(\tau/2) = 0$ imposes a reduction of the instantaneous cost of the CD term. The evolution of the position density of the system undergoing to the unitary dynamics with $\alpha^{\rm Q}_1$ and $\alpha^{\rm Q}_2$ is shown respectively in Figs. 5(b) and 5(c), along with the time-varying potential with the quantum protocol. As one can see,

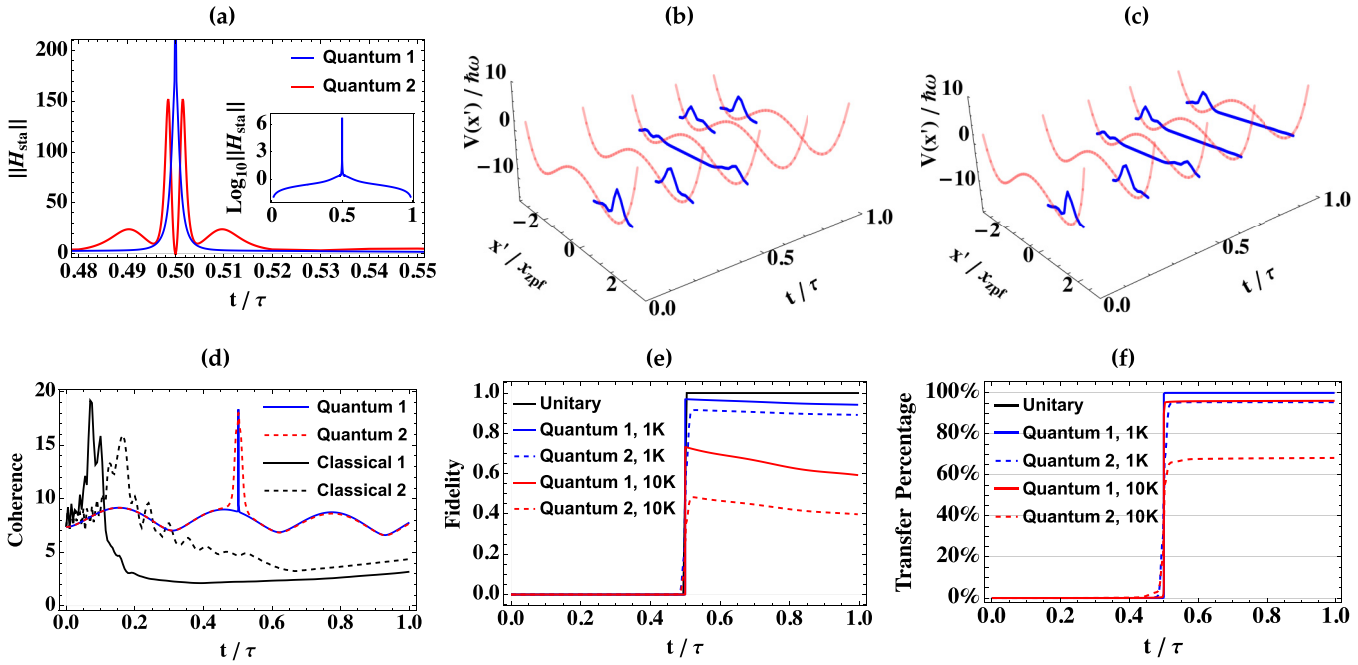

FIG. 5. The quantum state-transfer protocol. (a) The trace norm of the counterdiabatic driving term $H_{\rm STA}$, which is linked to the energetic cost [cf. Eq. (45)], in the vicinity of $t \simeq \tau/2$, where the overall dynamics is shown in the inset. [(b), (c)] The dynamics of the position density distribution of the system under the open dynamics at 1 K temperature, respectively for quantum protocols 1 and 2. (d) The coherence evolution for quantum protocol 1 (continuous blue line) and 2 (dashed red line) compared to the classical protocols 1 (continuous black) and 2 (dashed black). (e) The fidelity of the quantum protocols for the unitary dynamics (continuous black line) and for the open dynamics (continuous and dashed colored lines) at different temperatures. A fidelity smaller than 1 indicates that the state of the system is different from the target state, and that possibly only part of the system is transferred from one to the other well. This information is corroborated by the transfer percentage [cf. Eq. (44)], which is shown in (f).

the system is initially well localized in the right well. Then, at $t = \tau/2$, the state goes in a superposition of left and right states, and the position density delocalizes over both wells. Eventually, the system is fully transferred to the left well, where the system localizes again. In Fig. 5(d), we compare the dynamics of the coherence C_{l_1}, which is quantified with an l_1 measure in the basis of x' [94] as $C_{l_1}(\rho) = \sum_{j\neq k} |\rho_{jk}|$, for the unitary dynamics described by the two quantum protocols and with the two classical ones. The interaction with the environment reduces the performances of the protocol in two manners. First, as it is shown in Fig. 5(e), the fidelity between the final state ρ_f and the target state $\rho_{\rm TG}$ changes as a decreasing function of the temperature. Second, the environment inhibits the state transfer from one to the other well. In Fig. 5(f), we show the evolution of the transfer percentage [cf. Eq. (44)], which is the amount of population of the total state that has been transferred from the right to the left well. One can notice that the transfer percentage has a behavior being similar to that of the fidelity. Both the quantum protocols perform in a similar way, with negligible differences, under unitary evolution when it comes to the fidelity and transfer percentage. When comparing the transfer percentage with that of the classical protocols shown in Fig. 4f, one clearly sees that quantum protocols are more effective and faster (indeed for the quantum protocol $\tau\omega = 10$, while for the classical protocol one has $\tau\omega = 300$). Moreover, Figs. 5(e) and 5(f) show that quantum protocol 1 performs, in terms of fidelity and state transfer, better than protocol 2.

V. QUANTIFICATION OF THE PROTOCOL

Having introduced the classical and quantum protocols for the state transfer, we now quantify their performances by employing our protocol grading $\mathcal{G}$ defined in Eq. (1). For simplicity, in the following, we only consider the environment at the temperature of 1 K. Nevertheless, we report the relevant quantities to compute $\mathcal{G}$ also for the case of 10 K in Table II, and compare them with those for 1 K.

In Fig. 6(a), we show the energetic cost weighted by the Bures angle $\Lambda_\tau^{\rm hs}/\sin^2[\mathcal{L}(\rho_i, \rho_f)]$, which is defined in Eq. (6), against the timescale $\omega\tau$ of different protocols. The gray area identifies the region forbidden by the QSL. Its boundary is characterized by the value of $g_{\rm S} = 1$ [cf. Eq. (7)], which corresponds to $\Lambda_\tau^{\rm hs}/\sin^2[\mathcal{L}(\rho_i, \rho_f)] = 1/\omega\tau$. The closer the line of the protocol is to the gray region, the better $g_{\rm S}$. In this figure, we clearly see the advantages of quantum protocols against the classical ones for small processing times $\omega\tau < 1$. This is due to the fact that classical protocols fail to produce distinguishable states (i.e., $\sin^2[\mathcal{L}(\rho_i, \rho_f)] \sim 0$), while the quantum protocols are always able (i.e., $\sin^2[\mathcal{L}(\rho_i, \rho_f)] \sim 1$). On the other hand, for large processing times ($\omega\tau > 40$), although both kind of protocols almost always produce distinguishable states, the environmental effects become no longer negligible. Instead, we see that quantum advantages disappear and the classical protocols behave better than the quantum ones. Finally, for intermediate processing times ($1 < \omega\tau < 40$), the intertwined behaviors of lines fail to provide any useful information on their performances.

TABLE II. Comparison between the state-transfer protocols here considered and the corresponding protocol grading under the action of a 1 K and 10 K environment. In particular, we consider the energy cost weighted by Bures angle $\Lambda_\tau^{\rm hs}/\sin^2[\mathcal{L}(\rho_i,\rho_f)]$, the timescale $\omega\tau$, the irreversible entropy production $\Sigma_{\rm ir}$, the transfer percentage $P(x\leqslant 0)$, the speed cost $g_{\rm S}$, the quality cost $g_{\rm Q}$, and the thermodynamic cost $g_{\rm T}$. Finally, we show the protocol grading $\mathcal{G}$.

	Classical 1		Classical 2		Quantum 1		Quantum 2	
T	1 K	10 K	1 K	10 K	1 K	10 K	1 K	10 K
$\omega\tau$	300		300		10		10	
$\Lambda_\tau^{\rm hs}/\sin^2[\mathcal{L}(\rho_i,\rho_f)]$	0.13	0.08	0.20	0.07	2.20	1.72	2.06	1.33
$\Sigma_{\rm ir}$	1.37	2.36	2.23	4.33	0.10	0.47	0.10	0.46
$P(x\leqslant 0)$	82.39%	57.80%	91.54%	56.32%	99.98%	96.10%	95.45%	68.28%
$g_{\rm S}$	0.88	0.90	0.86	0.90	0.90	0.91	0.90	0.92
$g_{\rm Q}$	0.27	0.09	0.36	0.10	0.94	0.59	0.89	0.40
$g_{\rm T}$	0.25	0.09	0.11	0.01	0.90	0.63	0.90	0.63
$\mathcal{G}$	0.06	0.007	0.03	0.0009	0.76	0.34	0.72	0.23

In Fig. 6(b), we show the fidelity $F(\rho_\tau,\rho_{\rm TG})$ between the final state ρ_τ to the target state $\rho_{\rm TG}$ [cf. Eq. (11)] against the processing time $\omega\tau$. As it is expected, for short processing times, the quantum protocols can achieve the task perfectly, i.e., transferring the state while preserving the correct information, while the classical protocols fail completely. For long processing times, both quantum and classical protocols result in similar fidelity due to thermalization. One can notice that quantum protocol 1 performs better than quantum protocol 2 [where we imposed that $\dot{H}_0(\tau/2)=0$], while classical protocol 2 performs better than classical protocol 1 (since there is less tilting involved).

In Fig. 6(c), we show the irreversible entropy production $\Sigma_{\rm ir}$ [cf. Eq. (20)] against $\omega\tau$. It indicates how far the system is driven away from the reversible dynamics and it quantifies the thermodynamic cost $g_{\rm T}$. We see that the effects of the environment become prominent when $\omega\tau>1$.

Having computed all terms in the protocol grading $\mathcal{G}$ given by Eq. (1), we show in Fig. 7 the values of $\mathcal{G}$ for both the quantum and the classical protocols. For $\omega\tau<1$, we see a strong difference between the classical ($\mathcal{G}\sim 0$) and the quantum ($\mathcal{G}\sim 1$) protocols, which narrows for larger values of $\omega\tau$. This is due to the fact that quantum protocols well perform for time smaller that the decoherence time ($\tau_{\rm dec}\sim\hbar^2/\gamma m k_{\rm B}T\Delta_x^2\sim 0.7$, where we took Δ_x as the distance between the two minima of double-well potential), while the classical protocols perform better with a more adiabatic timescale ($\omega\tau\gg 1$).

VI. CONCLUSIONS

In this paper, we design the protocol grading $\mathcal{G}$ that depends on a finite set of fundamental physical quantities, and it is used as a figure of merit of the performances of a process, by taking into consideration the speed, the fidelity, and the thermodynamic cost of the transfer process. We compute the protocol grading for four different state-transfer protocols in a double-well potential. These transfer a quantum superposition from one well to the other. Such a process can be successfully performed by employing a quantum protocol with the help of the counterdiabatic driving, while with classical processes the information about the initial superposition is washed away. Furthermore, quantum processes allow a state transfer that is quicker and more accurate, which is reflected by higher value for the protocol grading parameter.

ACKNOWLEDGMENTS

We thank Steve Campbell for many useful discussions. We acknowledge financial support from the H2020-FETOPEN-2018-2020 project TEQ (Grant No. 766900), the DfE-SFI

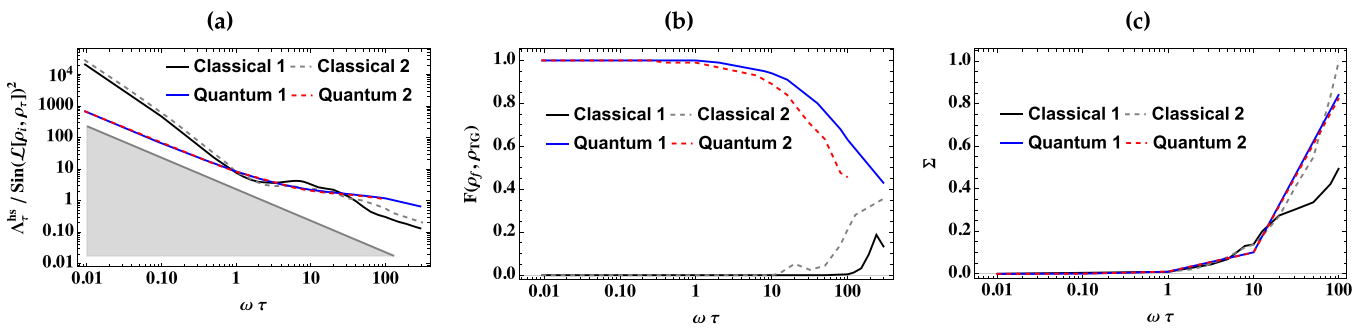

FIG. 6. Quantification of the state-transfer protocols for the two classical and two quantum protocols for the temperature of 1 K. (a) The relation between the inverse of the QSL ($\Lambda_\tau^{\rm hs}/\sin^2[\mathcal{L}(\rho_i,\rho_f)]$) and the processing time $\omega\tau$. The gray shaded region corresponds to the values of $\langle E\rangle_\tau$ and τ that violate the QSL. (b) The achieved fidelity $F(\rho_\tau,\rho_{\rm TG})$ for $\omega\tau=10$ for the quantum protocols and $\omega\tau=300$ for the classical ones. (c) The evolution of the irreversible entropy production rate Π.

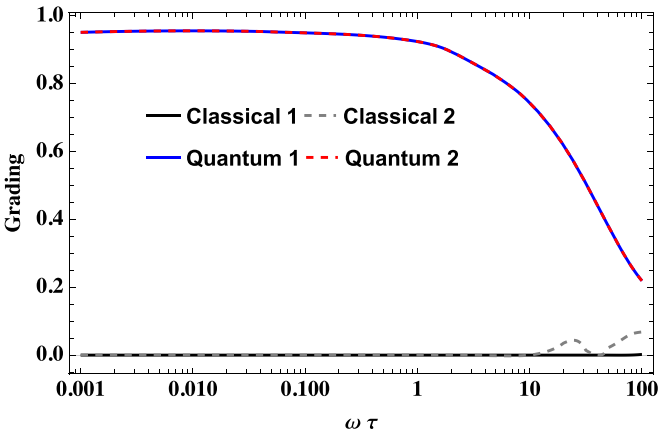

FIG. 7. The protocol grading $\mathcal{G}$ for the four considered state-transfer protocols under the action of the environment at 1 K at varying protocol timescale.

Investigator Programme (Grant No. 15/IA/2864), the Royal Society Wolfson Research Fellowship (RSWFR3183013), the Leverhulme Trust Research Project Grant (Grant No. RGP-2018-266), and the UK EPSRC (Grant No. EP/T028106/1) and the EU EIC Pathfinder project QuCoM (10032223). M.A.C. acknowledges support from the Österreichischer Wissenschaftsfonds FWF (M2915 Meitner program).

APPENDIX A: ANALOG WITH LANDAU-ZENER MODEL

The simplest analogy to our proposed model for the quantum protocol of the state transfer is given by the Landau-Zener model [95,96]. The model considers a two-level system with a Hamiltonian reading

$$H_{\rm LZ} = \Delta\sigma_z + g(t)\sigma_x, \tag{A1}$$

where Δ determines the minimal energy gap between the two energy levels, and $g(t)$ is a linear control function. In Fig. 8(a), we plot the eigenvalues of $H_{\rm LZ}$ in terms of g (continuous lines). As one can see, if we prepare initially the system in its ground state ($|-\rangle$) and then drive the system nonadiabatically by changing g, the system jumps from the ground state to the excited one ($|+\rangle$). This is most likely to happen when g is around zero, which corresponds to the minimum energy gap.

To circumvent the issue, we can introduce a counterdiabatic term to the original Hamiltonian [62,97]. The new Hamiltonian now reads

$$H_{\rm LZ}^{\rm new} = H_{\rm LZ} + H_{\rm STA}, \tag{A2}$$

where

$$H_{\rm STA} = -\frac{\dot{g}(t)\Delta}{2(\Delta^2 + g(t)^2)}\sigma_y. \tag{A3}$$

With such a counterdiabatic term, the ground-state trajectory becomes the finite-time solution of the new Hamiltonian $H_{\rm LZ}^{\rm new}$.

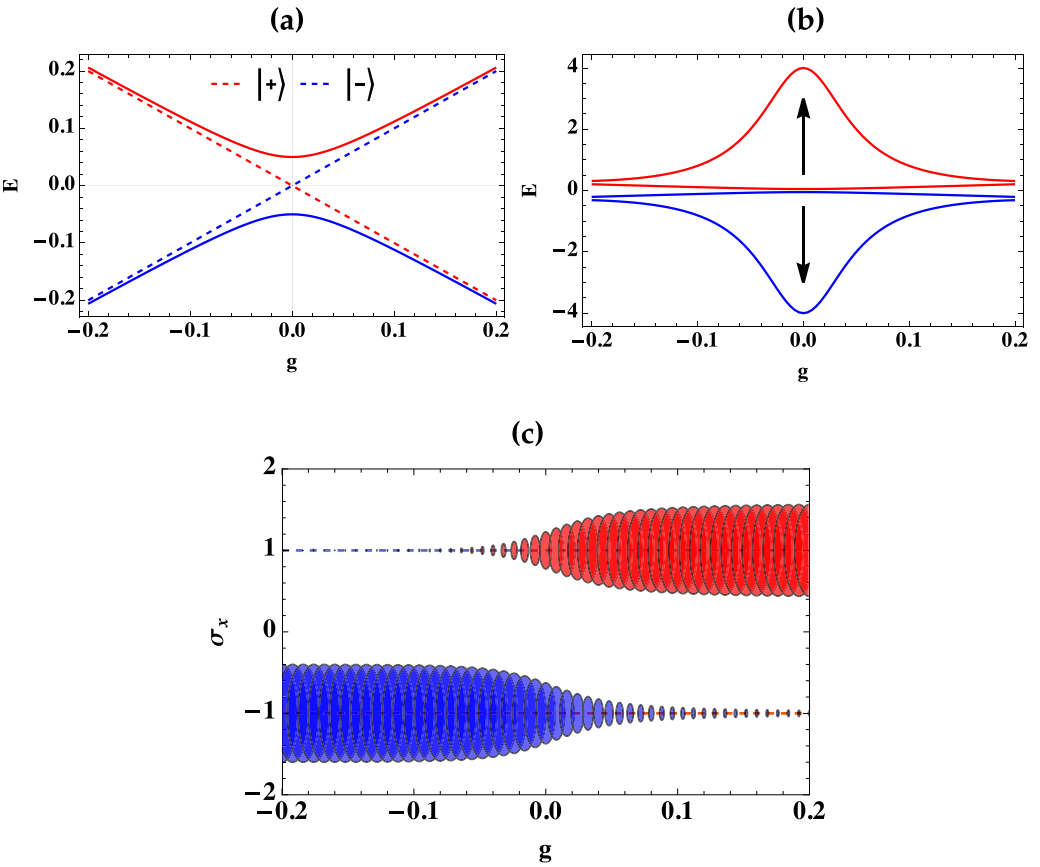

FIG. 8. Illustration of the state transfer with Landau-Zener model. (a) The change of energy against the tuning parameter g. (b) The change of energy for states $|+\rangle$ and $|-\rangle$ as the STA is implemented. (c) Population changes in the σ_x basis, if we prepare $|-\rangle$ as the initial state. Here we used $\Delta = 0.05$.

This is due to the increased energy gap imposed by H_{STA}, as indicated by the arrows in Fig. 8(b). The increased energy gap allows the system to remain in the ground state without jumping to the excited state as we change g. We underline that following the ground state (blue continuous line), one switches the state from $|-\rangle$ to $|+\rangle$ [dashed lines in Fig. 8(a)]. This is essentially the state transfer we want to simulate in our model. By changing the value of g in time, the population of the state $|-\rangle$ moves to the state $|+\rangle$. This is pictured in Fig. 8(c), where the dimensions of the colored disks represent the amount of population of the two states (blue for $|-\rangle$ and red for $|+\rangle$).

However, the dynamics looks differently if we consider the position of the system rather than the spin. Our framework imposes the relation between the position operator and the spin operator J_x based on the HP transformation. Taking this Landau-Zener model as an example, we can take σ_x as a close analog of the position operator, and monitor the population that changes in "positions," i.e., from -1 to $+1$ (corresponding to the eigenstates $|-\rangle$ and $|+\rangle$). If we prepare our initial state as $|-\rangle$, we can see the state transfers from one position to the other position, as shown in Fig. 8(c).

APPENDIX B: DECOMPOSE THE DISSIPATOR INTO REVERSIBLE AND IRREVERSIBLE PARTS

In this Appendix, we compute, along the lines of Ref. [78], the contributions to the entropy rates corresponding to the following term of the Caldeira-Leggett dissipator in Eq. (14):

$$D[\rho] = [x, \{p, \rho\}] = [x, f(\rho)], \tag{B1}$$

where $f[\rho] = f^{\dagger}[\rho] = \{p, \rho\}$. As $D[\rho]$ contains the operator x, we express the dissipator in the Husimi Q representation. In particular, the Husimi Q function is defined in Eq. (17) and we have the following correspondences [98]:

$$\begin{aligned} C_x[\rho] = [x, \rho] \ &\leftrightarrow C_x(Q) = \frac{1}{\sqrt{2}}(\partial_{\alpha^*} - \partial_{\alpha})Q, \\ C_p[\rho] = [p, \rho] \ &\leftrightarrow C_p(Q) = -\frac{i}{\sqrt{2}}(\partial_{\alpha^*} + \partial_{\alpha})Q, \\ f[\rho] = \{p, \rho\} \ &\leftrightarrow f(Q) = \frac{i}{\sqrt{2}}(2\alpha^* - 2\alpha - \partial_{\alpha^*} + \partial_{\alpha})Q, \end{aligned} \tag{B2}$$

where we define two currents $C_x(Q)$ and $C_p(Q)$. One can work out the reverse correspondences,

$$\begin{aligned} \partial_{\alpha} Q &= -\frac{1}{\sqrt{2}}(C_x(Q) - iC_p(Q)), \\ \partial_{\alpha^*} Q &= \frac{1}{\sqrt{2}}(C_x(Q) + iC_p(Q)), \end{aligned} \tag{B3}$$

and thus rewrite $f(Q)$ in terms of currents,

$$f(Q) = i\sqrt{2}(\alpha^* - \alpha)Q - iC_x(Q). \tag{B4}$$

With these correspondences, we can have the dissipator in phase space,

$$D[\rho] \ \leftrightarrow \ D(Q) = C_x(f(Q)). \tag{B5}$$

Given the definition of the Wehrl entropy in Eq. (16), we can rewrite its rate component corresponding to the term $D[\rho]$ as

$$\frac{dS}{dt} = \int d\alpha \int d\alpha^* \, \frac{1}{Q} f(Q) C_x(Q). \tag{B6}$$

Employing Eq. (B4), we get

$$\frac{dS}{dt} = i \int d\alpha \int d\alpha^* \, \underbrace{\sqrt{2}(\alpha^* - \alpha)C_x(Q)}_{\text{flux}} + \underbrace{\frac{1}{Q}|C_x(Q)|^2}_{\text{irreversible}}, \tag{B7}$$

where we use the correspondences, integrate by parts, and take $C_x(Q) = -C_x(Q)^*$. By working backwards, we find the corresponding decomposition in density matrix representation, which is given by

$$D[\rho] = -i[x, [x, \rho]] - i\sqrt{2}[x, \rho a - a^{\dagger}\rho], \tag{B8}$$

being Eq. (23) of the main text.

Now, the irreversible entropy production rate Π is associated with an even function of the current, and the entropy flux rate Φ is associated with an odd function of the current [70]. According to this argument, we can separate the Wehrl entropy rate into

$$\begin{aligned} \Pi &= i \int d\alpha \int d\alpha^* \, \frac{1}{Q}|C_x(Q)|^2, \\ \Phi &= i \int d\alpha \int d\alpha^* \, \sqrt{2}(\alpha - \alpha^*)C_x(Q), \end{aligned} \tag{B9}$$

which are respectively the irreversible entropy production rate and entropy flux rate.

[1] X.-B. Wang, T. Hiroshima, A. Tomita, and M. Hayashi, Quantum information with Gaussian states, Phys. Rep. **448**, 1 (2007).

[2] C. Weedbrook, S. Pirandola, R. Garcia-Patron, N. J. Cerf, T. C. Ralph, J. H. Shapiro, and S. Lloyd, Gaussian quantum information, Rev. Mod. Phys. **84**, 621 (2012).

[3] S. Yokoyama *et al.*, Ultra-large-scale continuous-variable cluster states multiplexed in the time domain, Nat. Photonics **7**, 982 (2013).

[4] J. Roslund, R. M. de Araújo, S. Jiang, C. Fabre, and N. Treps, Wavelength-multiplexed quantum networks with ultrafast frequency combs, Nat. Photonics **8**, 109 (2014).

[5] W. Asavanant *et al.*, Generation of time-domain-multiplexed two-dimensional cluster state, Science **366**, 373 (2019).

[6] V. Giovannetti, S. Lloyd, and L. Maccone, Quantum-enhanced measurements: Beating the standard quantum limit, Science **306**, 1330 (2004).

[7] S. Pirandola, B. R. Bardhan, T. Gehring, C. Weedbrook, and S. Lloyd, Advances in photonic quantum sensing, Nat. Photonics **12**, 724 (2018).

[8] N. Gisin and R. Thew, Quantum communication, Nat. Photonics **1**, 165 (2007).

[9] H.-S. Zhong *et al.*, Quantum computational advantage using photons, Science **370**, 1460 (2020).

[10] J. Chen, Review on quantum communication and quantum computation, J. Phys.: Conf. Ser. **1865**, 022008 (2021).

[11] A. S. Holevo, M. Sohma, and O. Hirota, Capacity of quantum Gaussian channels, Phys. Rev. A **59**, 1820 (1999).

[12] M. M. Wolf, G. Giedke, and J. I. Cirac, Extremality of Gaussian Quantum States, Phys. Rev. Lett. **96**, 080502 (2006).

[13] S. Lloyd and S. L. Braunstein, Quantum Computation over Continuous Variables, Phys. Rev. Lett. **82**, 1784 (1999).

[14] D. Gottesman, A. Kitaev, and J. Preskill, Encoding a qubit in an oscillator, Phys. Rev. A **64**, 012310 (2001).

[15] N. Lee *et al.*, Teleportation of nonclassical wave packets of light, Science **332**, 330 (2011).

[16] A. I. Lvovsky *et al.*, Production and applications of non-Gaussian quantum states of light, arXiv:2006.16985.

[17] M. Walschaers, Non-Gaussian quantum states and where to find them, Phys. Rev. X Quantum **2**, 030204 (2021).

[18] L. Amico *et al.*, Roadmap on atomtronics: State of the art and perspective, AVS Quantum Sci. **3**, 039201 (2021).

[19] J. Millen, T. S. Monteiro, R. Pettit, and A. N. Vamivakas, Optomechanics with levitated particles, Rep. Prog. Phys. **83**, 026401 (2020).

[20] B. Xu *et al.*, Nanomechanical resonators: Toward atomic scale, ACS Nano **16**, 15545 (2022).

[21] M. Kjaergaard *et al.*, Superconducting qubits: Current state of play, Annu. Rev. Condens. Matter Phys. **11**, 369 (2020).

[22] M. Novaes, Wigner and Husimi functions in the double-well potential, J. Opt. B: Quantum Semiclassical Opt. **5**, S342 (2003).

[23] E. Kierig, U. Schnorrberger, A. Schietinger, J. Tomkovic, and M. K. Oberthaler, Single-Particle Tunneling in Strongly Driven Double-Well Potentials, Phys. Rev. Lett. **100**, 190405 (2008).

[24] M. c. v. Gavrilov and J. Bechhoefer, Erasure without Work in an Asymmetric Double-Well Potential, Phys. Rev. Lett. **117**, 200601 (2016).

[25] S. Campbell, G. De Chiara, and M. Paternostro, Equilibration and nonclassicality of a double-well potential, Sci. Rep. **6**, 19730 (2016).

[26] Y. Shi, C. Chamberland, and A. Cross, Fault-tolerant preparation of approximate GKP states, New J. Phys. **21**, 093007 (2019).

[27] A. O. C. Davis, M. Walschaers, V. Parigi, and N. Treps, Conditional preparation of non-gaussian quantum optical states by mesoscopic measurement, New J. Phys. **23**, 063039 (2021).

[28] W.-L. Ma *et al.*, Quantum control of bosonic modes with superconducting circuits, Sci. Bull. **66**, 1789 (2021).

[29] L. Giannelli *et al.*, A tutorial on optimal control and reinforcement learning methods for quantum technologies, Phys. Lett. A **434**, 128054 (2022).

[30] C. P. Koch *et al.*, Quantum optimal control in quantum technologies. Strategic report on current status, visions and goals for research in Europe, Eur. Phys. J. Quantum Technol. **9**, 19 (2022).

[31] M. Frimmer, J. Gieseler, and L. Novotny, Cooling Mechanical Oscillators by Coherent Control, Phys. Rev. Lett. **117**, 163601 (2016).

[32] M. Rossi, D. Mason, J. Chen, Y. Tsaturyan, and A. Schliesser, Measurement-based quantum control of mechanical motion, Nature (London) **563**, 53 (2018).

[33] U. Delić *et al.*, Cooling of a levitated nanoparticle to the motional quantum ground state, Science **367**, 892 (2020).

[34] U. Boscain, M. Sigalotti, and D. Sugny, Introduction to the Pontryagin maximum principle for quantum optimal control, Phys. Rev. X Quantum **2**, 030203 (2021).

[35] A. del Campo and K. Kim, Focus on shortcuts to adiabaticity, New J. Phys. **21**, 050201 (2019).

[36] D. Guéry-Odelin, A. Ruschhaupt, A. Kiely, E. Torrontegui, S. Martinez-Garaot, and J. G. Muga, Shortcuts to adiabaticity: Concepts, methods, and applications, Rev. Mod. Phys. **91**, 045001 (2019).

[37] V. Giovannetti, S. Lloyd, and L. Maccone, Advances in quantum metrology, Nat. Photonics **5**, 222 (2011).

[38] K. Hammam, Y. Hassouni, R. Fazio, and G. Manzano, Optimizing autonomous thermal machines powered by energetic coherence, New J. Phys. **23**, 043024 (2021).

[39] W. Ji, Z. Chai, M. Wang, Y. Guo, X. Rong, F. Shi, C. Ren, Y. Wang, and J. Du, Spin Quantum Heat Engine Quantified by Quantum Steering, Phys. Rev. Lett. **128**, 090602 (2022).

[40] D. Stefanatos, Optimal shortcuts to adiabaticity for a quantum piston, Automatica **49**, 3079 (2013).

[41] V. Martikyan, D. Guéry-Odelin, and D. Sugny, Comparison between optimal control and shortcut to adiabaticity protocols in a linear control system, Phys. Rev. A **101**, 013423 (2020).

[42] Q. Zhang, X. Chen, and D. Guéry-Odelin, Connection between inverse engineering and optimal control in shortcuts to adiabaticity, Entropy **23**, 84 (2021).

[43] M. V. Berry, Transitionless quantum driving, J. Phys. A: Math. Theor. **42**, 365303 (2009).

[44] A. del Campo, Shortcuts to Adiabaticity by Counterdiabatic Driving, Phys. Rev. Lett. **111**, 100502 (2013).

[45] S. An, D. Lv, A. Del Campo, and K. Kim, Shortcuts to adiabaticity by counterdiabatic driving for trapped-ion displacement in phase space, Nat. Commun. **7**, 12999 (2016).

[46] D. Sels and A. Polkovnikov, Minimizing irreversible losses in quantum systems by local counterdiabatic driving, Proc. Natl. Acad. Sci. USA **114**, E3909 (2017).

[47] O. Abah, R. Puebla, and M. Paternostro, Quantum State Engineering by Shortcuts to Adiabaticity in Interacting Spin-Boson Systems, Phys. Rev. Lett. **124**, 180401 (2020).

[48] M. A. Simón, M. Palmero, S. Martínez-Garaot, and J. G. Muga, Trapped-ion Fock-state preparation by potential deformation, Phys. Rev. Res. **2**, 023372 (2020).

[49] S. Alipour, A. Chenu, A. T. Rezakhani, and A. del Campo, Shortcuts to adiabaticity in driven open quantum systems: Balanced gain and loss and non-Markovian evolution, Quantum **4**, 336 (2020).

[50] Z. Yin *et al.*, Shortcuts to adiabaticity for open systems in circuit quantum electrodynamics, Nat. Commun. **13**, 188 (2022).

[51] A. I. Lvovsky, B. C. Sanders, and W. Tittel, Optical quantum memory, Nat. Photonics **3**, 706 (2009).

[52] M. P. Hedges, J. J. Longdell, Y. Li, and M. J. Sellars, Efficient quantum memory for light, Nature (London) **465**, 1052 (2010).

[53] K. Heshami, D. G. England, P. C. Humphreys, P. J. Bustard, V. M. Acosta, J. Nunn, and B. J. Sussman, Quantum memories: Emerging applications and recent advances, J. Mod. Opt. **63**, 2005 (2016).

[54] Q. Wu, L. Mancino, M. Carlesso, M. A. Ciampini, L. Magrini, N. Kiesel, and M. Paternostro, Nonequilibrium quantum thermodynamics of a particle trapped in a controllable time-varying potential, Phys. Rev. X Quantum **3**, 010322 (2022).

[55] J. Goold, M. Huber, A. Riera, L. del Rio, and P. Skrzypczyk, The role of quantum information in thermodynamics—a topical review, J. Phys. A: Math. Theor. **49**, 143001 (2016).

[56] M. Schlosshauer, Quantum decoherence, Phys. Rep. **831**, 1 (2019).

[57] S. Deffner and S. Campbell, Quantum speed limits: From Heisenberg's uncertainty principle to optimal quantum control, J. Phys. A: Math. Theor. **50**, 453001 (2017).

[58] L. Mandelstam and I. Tamm, The uncertainty relation between energy and time in non-relativistic quantum mechanics, in *Selected Papers*, edited by B. Bolotovskii, V. Frenkel, and R. Peierls (Springer, Berlin, 1991).

[59] N. Margolus and L. B. Levitin, The maximum speed of dynamical evolution, Physica D **120**, 188 (1998).

[60] L. B. Levitin and T. Toffoli, Fundamental Limit on the Rate of Quantum Dynamics: The Unified Bound Is Tight, Phys. Rev. Lett. **103**, 160502 (2009).

[61] S. Deffner and E. Lutz, Quantum Speed Limit for Non-Markovian Dynamics, Phys. Rev. Lett. **111**, 010402 (2013).

[62] S. Campbell and S. Deffner, Trade-Off Between Speed and Cost in Shortcuts to Adiabaticity, Phys. Rev. Lett. **118**, 100601 (2017).

[63] Y. Zheng, S. Campbell, G. De Chiara, and D. Poletti, Cost of counterdiabatic driving and work output, Phys. Rev. A **94**, 042132 (2016).

[64] C. Gonzalez-Ballestero, P. Maurer, D. Windey, L. Novotny, R. Reimann, and O. Romero-Isart, Theory for cavity cooling of levitated nanoparticles via coherent scattering: Master equation approach, Phys. Rev. A **100**, 013805 (2019).

[65] E. Joos and H. D. Zeh, The emergence of classical properties through interaction with the environment, Z. Phys. B **59**, 223 (1985).

[66] A. Caldeira and A. Leggett, Path integral approach to quantum Brownian motion, Physica A **121**, 587 (1983).

[67] S. Gao, Dissipative Quantum Dynamics with a Lindblad Functional, Phys. Rev. Lett. **79**, 3101 (1997).

[68] A. Lampo, S. H. Lim, J. Wehr, P. Massignan, and M. Lewenstein, Lindblad model of quantum Brownian motion, Phys. Rev. A **94**, 042123 (2016).

[69] G. Homa, J. Z. Bernád, and L. Lisztes, Positivity violations of the density operator in the Caldeira-Leggett master equation, Eur. Phys. J. D **73**, 53 (2019).

[70] G. T. Landi and M. Paternostro, Irreversible entropy production: From classical to quantum, Rev. Mod. Phys. **93**, 035008 (2021).

[71] G. E. Crooks, Entropy production fluctuation theorem and the nonequilibrium work relation for free energy differences, Phys. Rev. E **60**, 2721 (1999).

[72] G. M. Wang, E. M. Sevick, E. Mittag, D. J. Searles, and D. J. Evans, Experimental Demonstration of Violations of the Second Law of Thermodynamics for Small Systems and Short Time Scales, Phys. Rev. Lett. **89**, 050601 (2002).

[73] C. Jarzynski and D. K. Wójcik, Classical and Quantum Fluctuation Theorems for Heat Exchange, Phys. Rev. Lett. **92**, 230602 (2004).

[74] K. Funo, M. Ueda, and T. Sagawa, Quantum fluctuation theorems, *Fundamental Theories of Physics* (Springer, Berlin, 2018), pp. 249–273.

[75] J. P. Santos, G. T. Landi, and M. Paternostro, Wigner Entropy Production Rate, Phys. Rev. Lett. **118**, 220601 (2017).

[76] S. Abe, Nonadditive generalization of the quantum Kullback-Leibler divergence for measuring the degree of purification, Phys. Rev. A **68**, 032302 (2003).

[77] K. M. R. Audenaert, Quantum skew divergence, J. Math. Phys. **55**, 112202 (2014).

[78] J. P. Santos, L. C. Céleri, F. Brito, G. T. Landi, and M. Paternostro, Spin-phase-space-entropy production, Phys. Rev. A **97**, 052123 (2018).

[79] M. Brunelli and M. Paternostro, Irreversibility and correlations in coupled quantum oscillators, arXiv:1610.01172.

[80] A. Bérut *et al.*, Experimental verification of Landauer's principle linking information and thermodynamics, Nature (London) **483**, 187 (2012).

[81] J. Hong, B. Lambson, S. Dhuey, and J. Bokor, Experimental test of Landauer's principle in single-bit operations on nanomagnetic memory bits, Sci. Adv. **2**, e1501492 (2016).

[82] M. A. Ciampini *et al.*, Experimental nonequilibrium memory erasure beyond Landauer's bound, arXiv:2107.04429.

[83] R. Landauer, Irreversibility and heat generation in the computing process, IBM J. Res. Dev. **5**, 183 (1961).

[84] M. Konopik, A. Friedenberger, N. Kiesel, and E. Lutz, Nonequilibrium information erasure below kT ln 2, Europhys. Lett. **131**, 60004 (2020).

[85] S. Campbell, G. De Chiara, M. Paternostro, G. M. Palma, and R. Fazio, Shortcut to Adiabaticity in the Lipkin-Meshkov-Glick Model, Phys. Rev. Lett. **114**, 177206 (2015).

[86] R. Gaudenzi, E. Burzurí, S. Maegawa, H. S. J. van der Zant, and F. Luis, Quantum Landauer erasure with a molecular nanomagnet, Nat. Phys. **14**, 565 (2018).

[87] A. Patra and C. Jarzynski, Shortcuts to adiabaticity using flow fields, New J. Phys. **19**, 125009 (2017).

[88] A. Patra and C. Jarzynski, Semiclassical fast-forward shortcuts to adiabaticity, Phys. Rev. Res. **3**, 013087 (2021).

[89] O. Abah *et al.*, Energetic cost of quantum control protocols, New J. Phys. **21**, 103048 (2019).

[90] A. Chatterjee, P. Stevenson, S. De Franceschi, A. Morello, N. P. de Leon, and F. Kuemmeth, Semiconductor qubits in practice, Nat. Rev. Phys. **3**, 157 (2021).

[91] F. Pistolesi, A. N. Cleland, and A. Bachtold, Proposal for a Nanomechanical Qubit, Phys. Rev. X **11**, 031027 (2021).

[92] L. Magrini, P. Rosenzweig, C. Bach, A. Deutschmann-Olek, S. G. Hofer, S. Hong, N. Kiesel, A. Kugi, and M. Aspelmeyer, Real-time optimal quantum control of mechanical motion at room temperature, Nature (London) **595**, 373 (2021).

[93] F. Tebbenjohanns, M. L. Mattana, M. Rossi, M. Frimmer, and L. Novotny, Quantum control of a nanoparticle optically levitated in cryogenic free space, Nature (London) **595**, 378 (2021).

[94] T. Baumgratz, M. Cramer, and M. B. Plenio, Quantifying Coherence, Phys. Rev. Lett. **113**, 140401 (2014).

[95] L. D. Landau, A theory of energy transfer. II, *Collected Papers of L.D. Landau*, edited by D. ter Haar (Pergamon, New York, 1965), pp. 63–66.

[96] C. Zener and R. H. Fowler, Non-adiabatic crossing of energy levels, Proc. R. Soc. London, Ser. A **137**, 696 (1932).

[97] X. Chen, I. Lizuain, A. Ruschhaupt, D. Guéry-Odelin, and J. G. Muga, Shortcut to Adiabatic Passage in Two- and Three-Level Atoms, Phys. Rev. Lett. **105**, 123003 (2010).

[98] C. W. Gardiner, *Quantum Noise*, edited by H. Haken (Springer-Verlag, Berlin, 1991).